Monthly Notices
of the
ROYAL ASTRONOMICAL SOCIETY

MNRAS **470,** 4739–4749 (2017)
Advance Access publication 2017 June 22

doi:10.1093/mnras/stx1576

Very massive stars, pair-instability supernovae and intermediate-mass black holes with the SEVN code

Mario Spera[1,2★] and Michela Mapelli[1,2]

[1] *INAF, Osservatorio Astronomico di Padova, Vicolo dell'Osservatorio 5, I-35122 Padova, Italy*
[2] *INFN, Milano Bicocca, Piazza della Scienza 3, I-20126 Milano, Italy*

Accepted 2017 June 19. Received 2017 June 19; in original form 2017 April 30

ABSTRACT

Understanding the link between massive ($\gtrsim$30 $\mathrm{M}_{\odot}$) stellar black holes (BHs) and their progenitor stars is a crucial step to interpret observations of gravitational-wave events. In this paper, we discuss the final fate of very massive stars (VMSs), with zero-age main sequence (ZAMS) mass $>$150 $\mathrm{M}_{\odot}$, accounting for pulsational pair-instability supernovae (PPISNe) and for pair-instability supernovae (PISNe). We describe an updated version of our population synthesis code SEVN, in which we added stellar evolution tracks for VMSs with ZAMS mass up to 350 $\mathrm{M}_{\odot}$ and we included analytical prescriptions for PPISNe and PISNe. We use the new version of SEVN to study the BH mass spectrum at different metallicity Z, ranging from $Z = 2.0 \times 10^{-4}$ to 2.0×10^{-2}. The main effect of PPISNe and PISNe is to favour the formation of BHs in the mass range of the first gravitational-wave event (GW150914), while they prevent the formation of remnants with mass 60–120 $\mathrm{M}_{\odot}$. In particular, we find that PPISNe significantly enhance mass-loss of metal-poor ($Z \leq 2.0 \times 10^{-3}$) stars with ZAMS mass $60 \leq M_{\mathrm{ZAMS}}/\,\mathrm{M}_{\odot} \leq 125$. In contrast, PISNe become effective only for moderately metal-poor ($Z < 8.0 \times 10^{-3}$) VMSs. VMSs with $m_{\mathrm{ZAMS}} \gtrsim 220$ $\mathrm{M}_{\odot}$ and $Z < 10^{-3}$ do not undergo PISNe and form intermediate-mass BHs (with mass $\gtrsim$200 $\mathrm{M}_{\odot}$) via direct collapse.

Key words: black hole physics – gravitational waves – methods: numerical – stars: mass-loss – supernovae: general.

1 INTRODUCTION

All three gravitational wave (GW) events detected so far by the advanced Laser Interferometer Gravitational-Wave Observatory (aLIGO) have been interpreted as the merger of a black hole (BH) binary (Abbott et al. 2016b,c; Abbott et al. 2017). Additionally, aLIGO identified another BH merger candidate (LVT151012) even though its significance is below the threshold to claim an unambiguous detection (Abbott et al. 2016a). The aLIGO detections demonstrated that stellar BH binaries (BHBs) exist and can merge within a Hubble time (Abbott et al. 2016d). Besides GW150914, GW151226 and GW170104, the confirmed stellar BHs are only few tens, most of them observed in Milky Way's X-ray binaries (Özel et al. 2010). Dynamical mass measurements in X-ray binaries, possible only for about a dozen of BHs, suggest a dearth of stellar BHs with mass $\gtrsim$15 $\mathrm{M}_{\odot}$ (Farr et al. 2011; Casares & Jonker 2014). In contrast, the masses of the two BHs in GW150914 (GW170104) are $36.2^{+5.2}_{-3.8}$ and $29.1^{+3.7}_{-4.4}$ $\mathrm{M}_{\odot}$ ($31.2^{+8.4}_{-6.0}$ and $19.4^{+5.3}_{-5.9}$ $\mathrm{M}_{\odot}$), respectively, and their merger formed a new BH with mass $62.3^{+3.7}_{-3.1}$ $\mathrm{M}_{\odot}$ ($48.7^{+5.7}_{-4.6}$ $\mathrm{M}_{\odot}$).

Inferring the properties of the progenitors of such massive BHs is still an open issue. The mass of a compact object is expected to strongly depend on the evolution of its progenitor and on the final supernova (SN) mechanism (Mapelli, Colpi & Zampieri 2009; Belczynski et al. 2010; Mapelli et al. 2013; Spera, Mapelli & Bressan 2015). In the last decade, the models of stellar winds underwent a major upgrade (Vink, de Koter & Lamers 2001; Gräfener & Hamann 2008; Vink et al. 2011; Muijres et al. 2012; Vink 2016), which radically changed the landscape of massive star evolution (e.g. Paxton et al. 2013, 2015; Chen et al. 2015). In particular, mass-loss by stellar winds solely determines the pre-SN mass (M_{fin}) of a star (Woosley, Heger & Weaver 2002), which is a crucial ingredient to understand its final fate.

While the physical mechanisms powering core-collapse SNe are still matter of debate (see Janka 2012 for a review), a dearth of observations of progenitor stars with zero-age main sequence (ZAMS) mass $M_{\mathrm{ZAMS}} \gtrsim 18$ $\mathrm{M}_{\odot}$ suggests that stars with a higher M_{ZAMS} might end their life quietly, without SN explosion (see Smartt 2015, and references therein). Several theoretical models (e.g. Fryer 1999; Fryer & Kalogera 2001; Mapelli et al. 2009; Fryer et al. 2012) predict the possibility that a star collapses directly to a BH if its final mass is large enough ($\gtrsim$30–40 $\mathrm{M}_{\odot}$, Spera et al. 2015). Alternative models suggest that the possibility of a direct collapse depends

---

★ E-mail: mario.spera@oapd.inaf.it

© 2017 The Authors
Published by Oxford University Press on behalf of the Royal Astronomical Society

on the innermost structure of a star at the onset of core-collapse (O'Connor & Ott 2011; Ertl et al. 2016). Regardless of the discrepancies between SN models, a direct collapse seems to be the only viable scenario to explain the masses of GW150914 with stellar BHs.

Most models of the BH mass spectrum include the effect of core-collapse SNe but neglect the impact of pair-instability SNe (PISNe, Fowler & Hoyle 1964) and pulsational PISNe (PPISNe), with few remarkable exceptions (Belczynski et al. 2016b; Woosley 2017). Unlike core-collapse SNe, the physical mechanism powering PISNe (Ober, El Eid & Fricke 1983; Bond, Arnett & Carr 1984; Heger et al. 2003; Woosley, Blinnikov & Heger 2007) and PPISNe (Barkat, Rakavy & Sack 1967; Woosley, Blinnikov & Heger 2007; Chen et al. 2014; Yoshida et al. 2016) is quite well understood: If the mass of the Helium core ($M_{\rm He,f}$) is $\gtrsim 30\,{\rm M}_{\odot}$, the formation of electron–positron pairs makes oxygen/silicon burn explosively. Recent hydrodynamical simulations (Woosley 2017) show that if $32\,{\rm M}_{\odot} \lesssim M_{\rm He,f} \lesssim 64\,{\rm M}_{\odot}$, the star undergoes several pulses that significantly enhance mass-loss before the star forms a compact remnant (PPISN), while if $64\,{\rm M}_{\odot} \lesssim M_{\rm He,f} \lesssim 135\,{\rm M}_{\odot}$, the ignition of oxygen and silicon releases enough energy to disrupt the entire star (PISN). If $M_{\rm He,f} \gtrsim 135\,{\rm M}_{\odot}$, the star is expected to avoid the PISN and to directly collapse.

Recently, Woosley (2017) investigated the onset of PPISNe for a grid of metal-poor stars ($Z \simeq 0.1\,{\rm Z}_{\odot}$) and for Helium-only stars. Woosley (2017, hereafter W17) shows that PPISNe are expected to occur for $70 \lesssim M_{\rm ZAMS}/\,{\rm M}_{\odot} \lesssim 150$, while PISNe are effective for very massive stars (VMSs, $150 \lesssim M_{\rm ZAMS}/\,{\rm M}_{\odot} \lesssim 260$). Stars with $M_{\rm ZAMS} \gtrsim 260\,{\rm M}_{\odot}$ are expected to avoid the PISN and possibly form intermediate-mass BHs (IMBHs).

The dependence of these limits on the adopted stellar evolution prescriptions is unclear. The major uncertainties come from the evolutionary models of VMSs ($M_{\rm ZAMS} \gtrsim 150\,{\rm M}_{\odot}$, see e.g. Heger et al. 2003). VMSs have been observed in extreme star-forming regions (e.g. Crowther et al. 2016) and might be the product of runaway collisions (i.e. multiple collisions in very dense stellar systems, Bonnell, Bate & Zinnecker 1998; Portegies Zwart et al. 1999). VMSs are promising candidates to explode as PISNe (Kozyreva et al. 2017). For instance, the luminosity curve of SN2007bi, SN 2213−1745 and SN 1000+0216 can be explained with a PISN model, assuming a progenitor star with a bare Helium core mass of $\sim 130\,{\rm M}_{\odot}$, and a ZAMS mass of $\sim 250\,{\rm M}_{\odot}$(Gal-Yam et al. 2009; Cooke et al. 2012). Furthermore, VMSs have also been claimed to be the progenitors of IMBHs (Portegies Zwart & McMillan 2002; Portegies Zwart et al. 2004; Freitag, Gürkan & Rasio 2006), but mass-loss by stellar winds seems to be a key ingredient to understand their fate (Giersz et al. 2015; Mapelli 2016). Vink et al. (2011) used a Monte Carlo approach to model the mass-loss rate of VMSs, but most stellar evolution codes do not include the Vink et al. (2011) prescriptions, with the remarkable exception of the PARSEC code (Padova And tRieste Stellar Evolution Code, Chen et al. 2015). As a consequence, the mass spectrum of heavy stellar BHs has been poorly investigated so far.

In this paper, we present an updated version of the Stellar EVolution for *N*-body (SEVN) population-synthesis code. The new version of SEVN includes (i) an analytic treatment for PPISNe and PISNe, and (ii) up-to-date evolutionary tracks for VMSs ($M_{\rm ZAMS}$ up to $350\,{\rm M}_{\odot}$, from Chen et al. 2015). We use the new version of SEVN to study the BH mass spectrum for different metallicities and for $M_{\rm ZAMS}$ up to $350\,{\rm M}_{\odot}$. We also discuss the impact of PPISNe and PISNe on the formation of the BHBs observed by aLIGO and on the possibility of forming IMBHs from VMSs.

2 METHOD

We updated SEVN (Spera et al. 2015) to investigate the effect of PPISNe and PISNe on the BH mass spectrum. SEVN reads pre-evolved stellar evolution tracks, generated for a grid of ZAMS masses and different metallicity to calculate the physical properties of stars. The stellar tracks are given in the form of input tables that SEVN interpolates on-the-fly. This approach makes SEVN versatile because it is possible to change stellar evolution prescriptions by substituting the input tables, without modifying the internal structure of the code.

In the last version of SEVN, we have introduced a new, non-linear method to interpolate stellar evolution tracks. The new scheme significantly improves the old, linear algorithm since it allows us to use less points in the input tables and, at the same time, it reduces the interpolation error. The details of the new interpolation method are shown in Appendix A.

The default version of SEVN includes a set of input tables generated using the PARSEC code (Bressan et al. 2012; Tang et al. 2014; Chen et al. 2015). The input tables range from metallicity $Z = 2.0 \times 10^{-4}$ to 2.0×10^{-2}, and each of them includes the evolutionary tracks of stars in the mass range $0.1 \le M_{\rm ZAMS}/\,{\rm M}_{\odot} \le 350$, with a mass step of $0.5\,{\rm M}_{\odot}$ (the upper mass limit was $150\,{\rm M}_{\odot}$ in the previous version of SEVN, Spera et al. 2015).

SEVN includes several up-to-date SN explosion prescriptions. Three of them (delayed, rapid and startrack models) are taken from Fryer et al. (2012) and use the final (pre-SN) Carbon–Oxygen core mass of the star ($M_{\rm CO,f}$) to distinguish between successful and failed SNe. The other two models are based on the compactness of the progenitor star at the onset of core collapse (O'Connor & Ott 2011; Ertl et al. 2016). The main difference between CO-based and compactness-based criteria is that the former has a net threshold (in terms of $M_{\rm ZAMS}$) between successful SNe and direct collapse, while the latter gives a more complex picture ('islands of direct collapse') since the compactness of the progenitor star does not vary monotonically with the pre-SN mass of the star.

Throughout this paper, if not specified otherwise, we adopt the delayed SN model from Fryer et al. (2012). This model predicts a successful SN, with fallback, for $M_{\rm CO,f} < 11\,{\rm M}_{\odot}$ and direct collapse for $M_{\rm CO,f} \ge 11\,{\rm M}_{\odot}$. To distinguish between NSs and BHs, we fix an upper limit for the maximum NS mass: We assume that all remnants with mass $M_{\rm rem} \ge 3\,{\rm M}_{\odot}$ are BHs (Oppenheimer & Volkoff 1939; Chamel et al. 2013). When an NS or a BH forms, we also take into account the mass-loss due to the emission of neutrinos. For NSs, we follow the approach of Timmes, Woosley & Weaver (1996), who estimate that the mass lost in neutrinos is at the level of $\sim 0.1 M_{\rm bar}$, where $M_{\rm bar}$ is the baryonic mass of the proto-compact object (see their equation 8). For BHs, we follow Fryer et al. (2012), who assume that BHs behave approximately the same way as NSs, so that the mass lost in neutrinos is simply fixed to $0.1 M_{\rm bar}$.

To account for PISNe and PPISNe, we adopt the following approach. Since SEVN is not an hydrodynamical code, we cannot simulate PPISNe and PISNe self-consistently. Still, we can use an analytical prescription that, starting from the physical properties of a star at a given time, mimics the mass-loss due to PPISNe and PISNe.

The prescriptions implemented in SEVN are based on the recent results obtained by W17. We obtained a formula that fits the values of the compact remnant masses given in tables 1 and 2 of W17 with a relative error $\lesssim 5$ per cent. Table 1 of W17 shows the

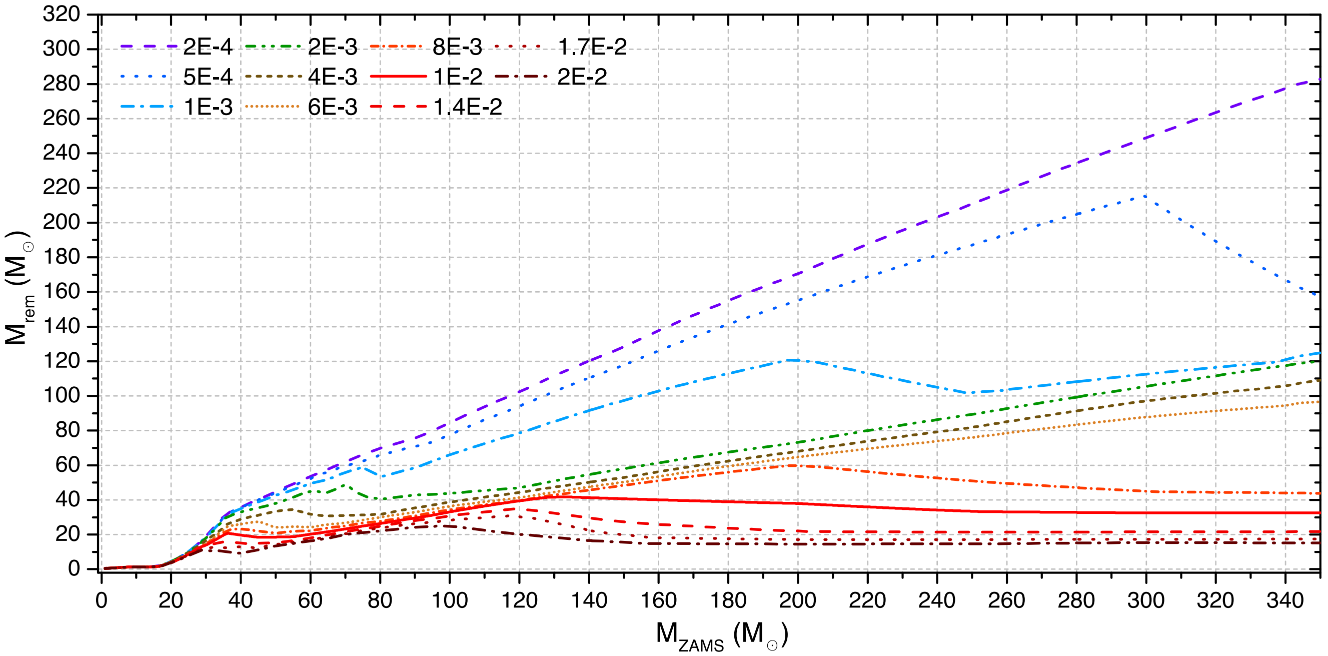

Figure 1. Mass of the compact remnant ($M_{\rm rem}$) as a function of the ZAMS mass of the star ($M_{\rm ZAMS}$), derived with SEVN, without PPISNe and PISNe. From bottom to top: dash-dotted brown line: $Z = 2.0 \times 10^{-2}$; dotted dark orange line: $Z = 1.7 \times 10^{-2}$; dashed red line: $Z = 1.4 \times 10^{-2}$; solid red line: $Z = 1.0 \times 10^{-2}$; short dash-dotted orange line: $Z = 8.0 \times 10^{-3}$; short dotted light orange line: $Z = 6.0 \times 10^{-3}$; short dashed line: $Z = 4.0 \times 10^{-3}$; dash-double dotted line: $Z = 2.0 \times 10^{-3}$; dash-dotted light blue line: $Z = 1.0 \times 10^{-3}$; dotted blue line: $Z = 5.0 \times 10^{-4}$; dashed violet line: $Z = 2.0 \times 10^{-4}$.

outcome of the explosion of Helium-only stars and table 2 is for ordinary stars at low metallicity ($Z \simeq 0.1\,\mathrm{Z}_{\odot}$). In table 2, different mass-loss prescriptions have been adopted to mimic the results for lower metallicity. Table 1 includes Helium stars with mass between 30 and 64 $\mathrm{M}_{\odot}$. Table 2 shows the evolution of progenitor stars with $70 \le M_{\rm ZAMS}/\mathrm{M}_{\odot} \le 150$, corresponding to $30 \lesssim M_{\rm He,f}/\mathrm{M}_{\odot} \lesssim 70$. In absence of PPISNe and PISNe, all these stars would have collapsed directly to massive BHs, losing only a small fraction of their final mass because of neutrino emission ($\sim 0.1 M_{\rm fin}$).

In SEVN, we adopt a fitting formula for the parameter as

$$\alpha_{\rm P} \equiv \frac{M_{\rm rem}}{M_{\rm rem,no\,psn}}, \qquad (1)$$

where $M_{\rm rem,no\,psn}$ is the mass of the compact remnant we would obtain without PPISNe and PISNe. We express $\alpha_{\rm P}$ as a function of the final Helium mass fraction of the star ($\mathcal{F} \equiv \frac{M_{\rm He,f}}{M_{\rm fin}}$) and $M_{\rm He,f}$. We obtain the mass of the compact remnant as $M_{\rm rem} = \alpha_{\rm P} M_{\rm rem,\,no\,psn}$, from equation (1). In particular, $\alpha_{\rm P} = 1$ for remnants that form via direct collapse and $\alpha_{\rm P} = 0$ for PISNe. The complete fitting formula is given in Appendix B.

The updated version of SEVN, including PISNe and PPISNe, is freely available for download at the following web address http://web.pd.astro.it/mapelli/group.html#software. An open access GitLab repository is available at: https://gitlab.com/mario.spera/SEVN.

In this paper, we use SEVN as a stand-alone code for population synthesis calculations but it can also be coupled with a large variety of *N*-body codes. We have already included SEVN in the STARLAB software environment (Portegies Zwart et al. 2001; Spera, Mapelli & Jeffries 2016) and in an updated version of the HIGPUS code (Capuzzo-Dolcetta, Spera & Punzo 2013), called HIGPUS-R. Preliminary access to the GitLab repository of HIGPUS-R is available upon request through the e-mail: mario.spera@live.it.

3 RESULTS

Fig. 1 shows the mass of the compact remnant as a function of the ZAMS mass of the progenitor star, for metallicity *Z* ranging from 2.0×10^{-4} to 2.0×10^{-2}. In SEVN and throughout this paper, we use $\mathrm{Z}_{\odot} = 0.01524$ for solar metallicity (Caffau et al. 2011). Thus, the metallicity range in Fig. 1 corresponds to 0.013–1.312 $\mathrm{Z}_{\odot}$. Fig. 1 is an updated version of fig. 6 of Spera et al. (2015), extending the maximum considered ZAMS mass from 150 to 350 $\mathrm{M}_{\odot}$ (using the evolutionary tracks from Chen et al. 2015). Fig. 1 does not include the effect of PPISNe and PISNe. The maximum BH mass we obtain in this case is $\sim 280\,\mathrm{M}_{\odot}$ at $Z = 2.0 \times 10^{-4}$, from a progenitor star with $M_{\rm ZAMS} \simeq 350\,\mathrm{M}_{\odot}$.

In Fig. 1, we adopt the delayed SN model. It is worth noting that, for stars with $M_{\rm ZAMS} \gtrsim 40\,\mathrm{M}_{\odot}$, the mass of the BH does not depend on the adopted core-collapse SN explosion model but only on: (i) the effectiveness of stellar winds, and (ii) the mass-loss due to the escape of neutrinos at the onset of core collapse. Using the PARSEC evolutionary models, all stars with $M_{\rm ZAMS} \gtrsim 40\,\mathrm{M}_{\odot}$ undergo direct collapse, since they have $M_{\rm CO,f} \gtrsim 11\,\mathrm{M}_{\odot}$.

Fig. 2 is the same as Fig. 1, but here we switched on PPISNe and PISNe. Both PPISNe and PISNe do not affect metal-rich stars. PPISNe first appear at $Z \le 10^{-2} \simeq 0.7\,\mathrm{Z}_{\odot}$ and their effects become significant at $Z \lesssim 2.0 \times 10^{-3}$, for stars with $60 \lesssim M_{\rm ZAMS}/\mathrm{M}_{\odot} \lesssim 125$. From Fig. 2, it is apparent that the main effect of PPISNe is to lower the curves of Fig. 1 and to enhance the formation of BHs in the mass range $30 \lesssim M_{\rm rem}/\mathrm{M}_{\odot} \lesssim 50$.

PISNe affect stars with metallicity $Z \le 8.0 \times 10^{-3} \simeq 0.5\,\mathrm{Z}_{\odot}$. Stars with $M_{\rm ZAMS} \gtrsim 210\,\mathrm{M}_{\odot}$, at $Z = 8.0 \times 10^{-3}$, do not undergo the

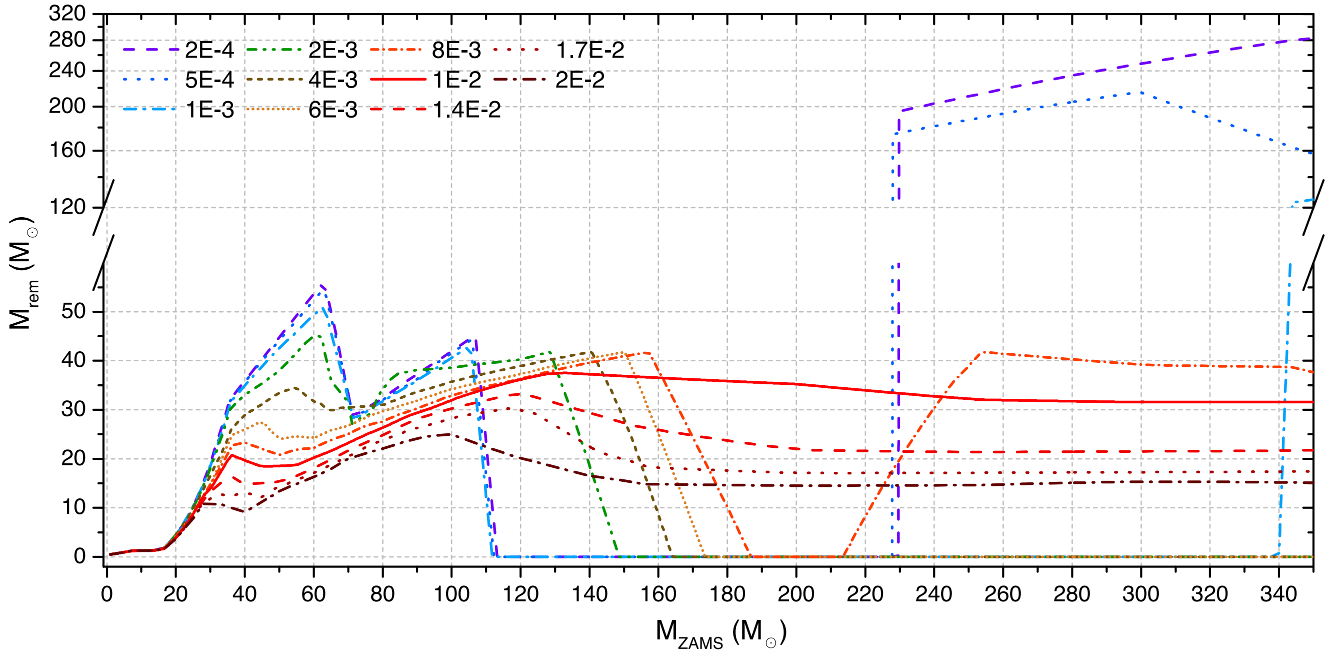

Figure 2. The same as Fig. 1 but with PPISNe and PISNe. We have inserted a y-axis break between 65 and 120 $\rm M_\odot$ because we have no BHs in this mass range.

PISN because such VMSs are close to their Eddington's luminosity. Thus, they lose a larger fraction of mass than lighter stars and they cannot reach $M_{\rm He,f} \simeq 64\,{\rm M}_\odot$ (i.e. the lower limit to activate the PISN mechanism).

Considering only stars with $M_{\rm ZAMS} \lesssim 200\,{\rm M}_\odot$, the maximum BH mass we obtain with PPISNe and PISNe is $\sim 55\,{\rm M}_\odot$ at $Z \simeq 2.0 \times 10^{-4} \simeq 0.01\,{\rm Z}_\odot$. Very massive BHs (120–280 $\rm M_\odot$) can form from the direct collapse of VMSs with $M_{\rm ZAMS} \gtrsim 200\,{\rm M}_\odot$ at $Z \lesssim 10^{-3} \simeq 0.07\,{\rm Z}_\odot$. Such massive stars have $M_{\rm He,f} \gtrsim 135\,{\rm M}_\odot$ and avoid PISNe. BHs with mass $\gtrsim 120\ {\rm M}_\odot$ are in the mass range of IMBHs.

Another effect of PPISNe and PISNe is that there is a dearth of compact remnants in the mass range between ~ 60 and $\sim 120\,{\rm M}_\odot$. This is apparent in Fig. 2, where we have inserted a y-axis break, corresponding to this range of BH masses. This result is in agreement with the mass gap found by Belczynski et al. (2016b) and W17. In Appendix C, we compare our results with those obtained by Woosley (2017).

In Appendix D, we provide detailed tables with the values of the most relevant quantities that have been used to produce Figs 1 and 2 (namely ZAMS mass, final mass, Helium core mass, CO mass, and remnant mass with and without PPISNe and PISNe) for three different metallicities ($Z = 2.0 \times 10^{-2}$, 2.0×10^{-3} and 2.0×10^{-4}).

Fig. 3 shows the remnants of massive single stars in the Z–$M_{\rm ZAMS}$ plane. Fig. 3 is an updated version of fig. 1 of Heger et al. (2003) that shows the regions where PPISNe (green area) and PISNe (red area) occur, and the region where neutrino-driven SNe and fallback mechanism take place (blue area). The hatched area is where stars undergo direct collapse. It is worth noting that all the stars that undergo the PPISN form compact remnants via direct collapse. The reason is that PPISNe enhance mass-loss from the stars' external layers leaving the Carbon–Oxygen core unaffected. Thus, such stars have always $M_{\rm CO,f} \gtrsim 11\,{\rm M}_\odot$, which is the lower limit for a failed SN in the delayed mechanism. This figure also shows that the lower limit in terms of $M_{\rm ZAMS}$ for direct collapse depends on metallicity. This limit is $\sim 35\,{\rm M}_\odot$ for $Z \le 1.6 \times 10^{-2}$ and it grows up to $\sim 50\,{\rm M}_\odot$ at $Z = 2.0 \times 10^{-2}$. A difference with fig. 1 of Heger et al. (2003) is that in Fig. 3 we show the area where PPISNe occur. Furthermore, it is worth noting that we do not form NSs or BHs by fallback from stars with $M_{\rm ZAMS} \gtrsim 50\,{\rm M}_\odot$. This is a consequence of the up-to-date prescriptions of stellar winds implemented in the parsec code that predict $M_{\rm CO,f} \gtrsim 11\,{\rm M}_\odot$ for $M_{\rm ZAMS} \gtrsim 50\,{\rm M}_\odot$, at any metallicity.

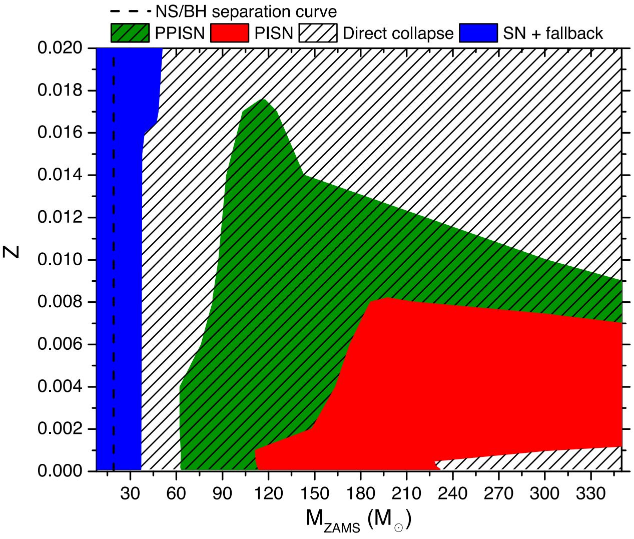

Figure 3. Regions of the Z–$M_{\rm ZAMS}$ plane where different SN mechanisms take place. Stars in the blue area end their life through a core-collapse SN with fallback. PPISNe and PISNe occur in the green and in the red area, respectively. The hatched area indicates direct collapse. The vertical dashed line at $M_{\rm ZAMS} \simeq 19\,{\rm M}_\odot$ divides stars that collapse into BHs ($M_{\rm ZAMS} \gtrsim 19\,{\rm M}_\odot$) from those forming NSs ($M_{\rm ZAMS} \lesssim 19\,{\rm M}_\odot$).

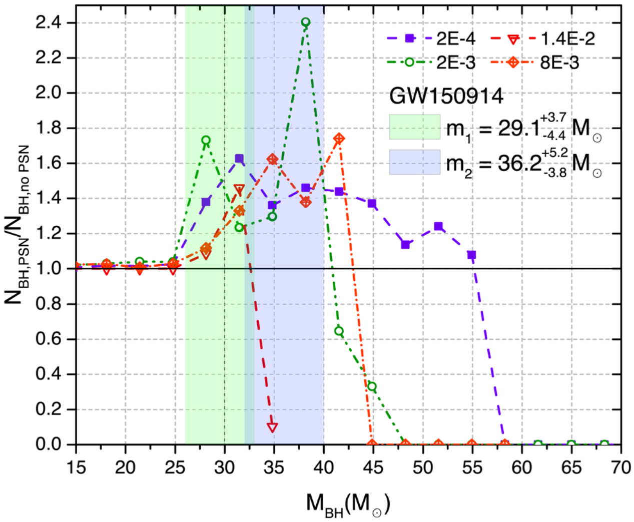

Figure 4. Ratio between the number of BHs obtained in the population synthesis simulations of set-A and set-B, respectively, as a function of the BH mass, and for different metallicity. To construct this figure, all the BHs in the mass range 3–80 $\mathrm{M}_\odot$ have been gathered into 20 mass bins. The abscissa of each point is the middle point of each mass bin. The green and blue shaded areas represent the masses of the two BHs of GW150914 with the associated uncertainties. Line types are the same as in Fig. 1 and indicate different metallicities.

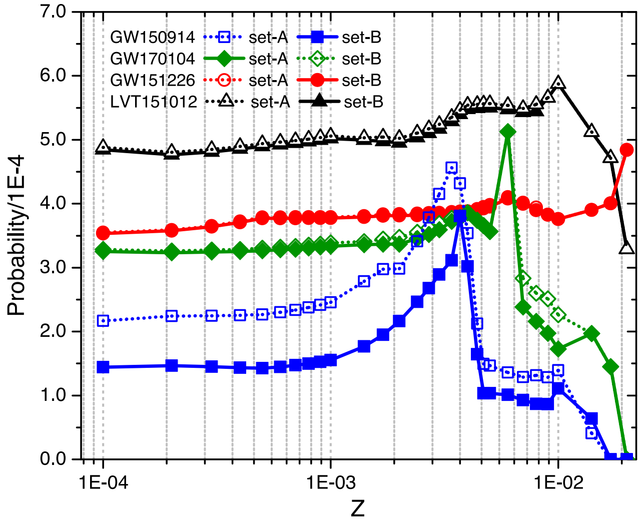

Figure 5. Relative probability, normalized to 10^{-4}, to obtain BH pairs like those observed by aLIGO in its observing runs, as a function of metallicity. Empty symbols connected through dashed lines show the results obtained from the simulations of set-A, while filled symbols connected with solid lines refer to simulations of set-B. We use blue squares for GW150914, green rhombi for GW170104, red circles for GW151226 and black triangles for LVT151012.

4 DISCUSSION

In this section, we discuss the impact of PISNe and PPISNe on the detected GW events and on the formation of IMBHs.

4.1 Formation environment of the gravitational-wave detections

To test the impact of PISNe and PPISNe on GW events, we performed two sets of population synthesis simulations which we refer to as set-A and set-B. Each set consists of 30 simulations at different metallicity in the range between $Z = 1.0 \times 10^{-4}$ and 2.0×10^{-2}. The number of stars in each run is 10^8. We verified that this number of objects is high enough to filter out statistical fluctuations in the analysis. All stars evolve in isolation for $\Delta t = 150$ Myr, which is a sufficiently long time to ensure that all the BHs have formed. The initial masses of the stars are sampled from a broken power-low mass function (Kroupa 2001), with a range $0.1 < M_{\mathrm{ZAMS}}/\mathrm{M}_\odot < 150$, and with slopes $\alpha_1 = 1.3$ for $0.1 \le m/\mathrm{M}_\odot < 0.5$ and $\alpha_2 = 2.3$ for $0.5 \le m/\mathrm{M}_\odot \le 150$. The only difference between set-A and set-B is that PPISNe and PISNe have been switched off in set-B.

Fig. 4 shows the ratio between the number of BHs we obtained from the simulations of set-A and that obtained from the simulations of set-B, as a function of the BH mass, for different values of metallicity. It is apparent that PPISNe favour the formation of BHs with masses between $\simeq$25 and $\simeq$50 $\mathrm{M}_\odot$. This result applies to a wide range of metallicities ($2.0 \times 10^{-4} \lesssim Z \lesssim 1.4 \times 10^{-2}$). For $Z \gtrsim 2.0 \times 10^{-2}$, neither PPISNe nor PISNe are effective so set-A and set-B generate the same results. In Fig. 4, we also show the masses of the two BHs of GW150914 and their associated uncertainties. In set-A, we form from $\sim$1.5 to $\sim$2.4 times more GW150914-like BHs than in the simulations of set-B. This result also applies to the primary BH of GW170104. In contrast, the effect of PISNe is to reduce the number of massive BHs in the runs of set-A. The maximum BH mass depends on metallicity and it is $\simeq$35, 45, 48, 60 $\mathrm{M}_\odot$ for $Z \simeq 1.4 \times 10^{-2}$, 8.0×10^{-3}, 2.0×10^{-3} and 2.0×10^{-4}, respectively.

From our runs, we can estimate the most probable metallicity of the formation environment of GW detections. For GW150914, in both sets of runs and for each value of metallicity, we counted the number of BHs (n_1) with mass $26 \le m_{\mathrm{BH}}/\mathrm{M}_\odot \le 33$ and those (n_2) with mass $32 \le m_{\mathrm{BH}}/\mathrm{M}_\odot \le 40$. These two mass ranges are the confidence intervals for the BH masses of GW150914 (see e.g. Abbott et al. 2016a). We divided the numbers n_1 and n_2 by the total number of simulated stars (10^8) to obtain the relative probability [$P(n_1)$ and $P(n_2)$, respectively] to form the two BHs in our simulations. The final probability to obtain a pair of GW150914-like BHs is then $P(n_1, n_2) \equiv \min(P(n_1), P(n_2))$. Similarly, we construct the same quantity for GW170104, GW151226 and LVT151012. We stress that our definition of $P(n_1, n_2)$ contains severe approximations because it does not account for either binary evolution processes or dynamical interactions.

Fig. 5 shows $P(n_1, n_2)$, normalized to 10^{-4}, as a function of metallicity, for the four GW events, obtained from the simulations of set-A and set-B. Fig. 5 indicates that in both sets of simulations, the probability curve of GW150914 favours low-metallicity with respect to high-metallicity environments. The curve peaks at about $3 \times 10^{-3} \lesssim Z \lesssim 4 \times 10^{-3}$ and rapidly decreases for $Z > 4 \times 10^{-3}$, becoming zero for $Z \gtrsim 1.7 \times 10^{-2}$. At $Z \gtrsim 1.7 \times 10^{-2}$, stellar winds become very effective, preventing the formation of BHs with mass above $\sim$25 $\mathrm{M}_\odot$ (see Fig. 2). From Fig. 5, we argue that the progenitors of GW150914 likely formed in a metal-poor environment with metallicity $Z \lesssim 4.0 \times 10^{-3} \simeq 0.3\ \mathrm{Z}_\odot$. This result is in agreement with the findings of Abbott et al. (2016d) and Belczynski et al. (2016a).

The probability curve of GW170104 is similar to that of GW150914. We obtain a maximum formation probability at about $6.0 \times 10^{-3}\ Z \lesssim Z \lesssim 7.0 \times 10^{-3}$. The curve rapidly decreases at higher metallicity, becoming zero at $Z = 2.0 \times 10^{-2}$, and

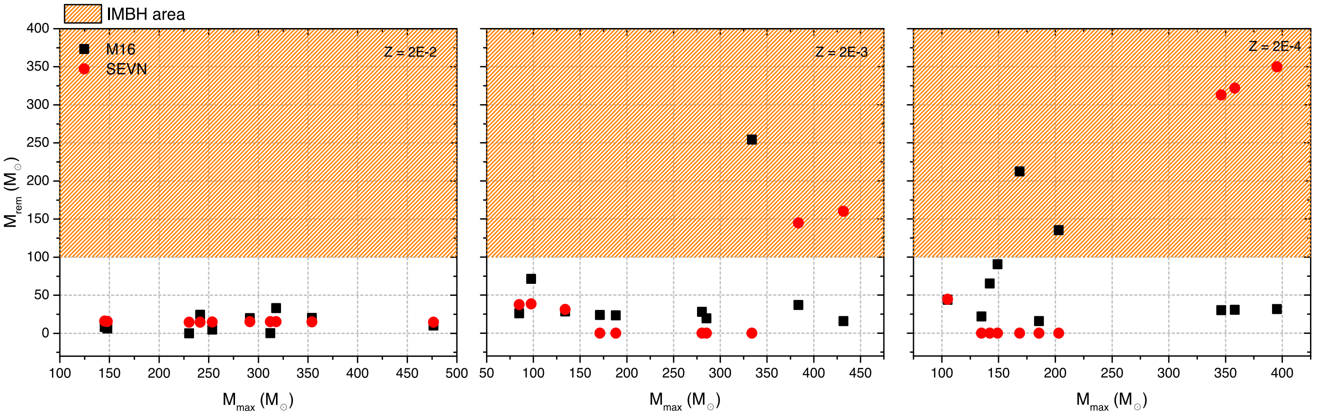

Figure 6. Mass of the compact remnant as a function of the maximum mass of the PCP. Black squares: simulations of Mapelli (2016); red circles: this work. Left-hand panel: $Z = 2.0 \times 10^{-2}$; middle panel: $Z = 2.0 \times 10^{-3}$; right-hand panel: $Z = 2.0 \times 10^{-4}$. The orange shaded region is the mass range of IMBHs ($>100\,\mathrm{M}_\odot$).

flattens for $Z \lesssim 5.0 \times 10^{-3}$. Thus, we can argue that GW170104 is likely formed in a metal-poor environment with metallicity $Z \lesssim 7.0 \times 10^{-3} \simeq 0.5\,\mathrm{Z}_\odot$.

The BHs observed in GW151226 are lighter ($m_1 = 14^{+8}_{-4}\,\mathrm{M}_\odot$, $m_2 = 7.5^{+2}_{-2}\,\mathrm{M}_\odot$). Since our models predict the formation of such BHs at every metallicity (see Fig. 2), the probability curve of GW151226 shown in Fig. 5 (red circles) is almost flat. High values of metallicity ($Z \gtrsim 10^{-2}$) are slightly favoured because, in metal–rich environments, all progenitor stars form BHs with masses below $\sim 25\,\mathrm{M}_\odot$. Furthermore, the probability curve obtained from set-A and set-B are overlapped. This happens because PPISNe and PISNe do not affect the formation of BHs with mass below $\sim 25\,\mathrm{M}_\odot$ (see Fig. 2). Fig. 5 also shows the probability curve of LVT151012 ($m_1 = 23^{+18}_{-6}\,\mathrm{M}_\odot$, $m_2 = 13^{+5}_{-5}\,\mathrm{M}_\odot$).

4.2 Formation of intermediate-mass black holes

The existence of IMBHs (mass between $\sim$100 and $\sim 10^5\,\mathrm{M}_\odot$) is still matter of debate (Farrell et al. 2009; Strader et al. 2012; Lanzoni et al. 2013; Lützgendorf et al. 2013; Baumgardt 2017; Kızıltan, Baumgardt & Loeb 2017; Zocchi, Gieles & Hénault-Brunet 2017).

From a theoretical point of view, several possible formation mechanisms have been proposed (e.g. Giersz et al. 2015, and references therein). One of them is the so-called runaway collision scenario: In a dense stellar system, a massive star (with mass $>100\,\mathrm{M}_\odot$) may form through a series of collisions and then may directly collapse into an IMBH (Portegies Zwart & McMillan 2002; Portegies Zwart et al. 2004). Recently, Mapelli (2016) has studied the impact of stellar winds on the formation of IMBHs from runaway collisions. Mapelli (2016) performed a set of direct *N*-body simulations of star clusters by means of the STARLAB software environment (Portegies Zwart et al. 2001). Stellar evolution was modified to include metallicity dependence and recent prescriptions for stellar winds, as described in Mapelli et al. (2013). Mapelli (2016) considered three different metallicities ($Z = 2.0 \times 10^{-2}$, 2.0×10^{-3} and 2.0×10^{-4}), performing, for each metallicity, ten different realizations of the same cluster (with 10^5 stars). The evolution of the principal collision product (PCP), defined as the product of the first collision that occurs in a simulated star cluster, is tracked in each simulation.

Mapelli (2016) finds that no IMBH can form at solar metallicity, because of the enhanced mass loss, whereas runaway collisions might still produce IMBHs at metallicity $\lesssim 0.1\ \mathrm{Z}_\odot$. The simulations of Mapelli (2016) do not include PPISNe and PISNe and adopt mass-loss prescriptions for VMSs that are extrapolated from formulas derived for 'ordinary' massive stars ($\sim$30–150 $\mathrm{M}_\odot$, Mapelli et al. 2013). Our aim is to check what is the impact of (i) the new stellar tracks for VMSs and of (ii) PPISNe and PISNe on the runaway collision products simulated by Mapelli (2016). Thus, we have re-run each PCP simulated by Mapelli (2016). We use SEVN including PPISNe and PISNe as described in Section 2. We start the evolution of each PCP with SEVN from the time when it reaches its maximum mass (see figs 2, 3 and 4 of Mapelli 2016). In the new evolution of the PCP, we apply self-consistent stellar evolutionary models (Chen et al. 2015) for stars with mass $\lesssim 350\,\mathrm{M}_\odot$, and we use a linear extrapolation of the curves shown in Fig. 2 for more massive stars. The main approximation of our approach is that we do not account for collisions occurring after the PCP has reached its maximum mass.

Fig. 6 compares the compact-object masses obtained with SEVN and those reported in Mapelli (2016) as a function of the maximum mass reached by the PCP. The three panels are for three different values of metallicity. For $Z = 2.0 \times 10^{-2}$, the two sets of points distribute approximately in the same $M_{\rm rem}$ range. The mass of the compact object formed by the PCP is always below $\sim 35\,\mathrm{M}_\odot$. At this high metallicity, mass-loss through stellar winds is effective so even VMSs may end their lives with no more than $\sim 40\,\mathrm{M}_\odot$, preventing the formation of IMBHs. At lower metallicity, we find several differences between SEVN and Mapelli (2016).

At $Z = 2.0 \times 10^{-3}$, one PCP in Mapelli (2016) reaches a maximum mass of $\sim 335\,\mathrm{M}_\odot$. In Mapelli (2016), this object undergoes direct collapse, forms a massive BH with mass $\sim 210\,\mathrm{M}_\odot$, and becomes an object of mass $\sim 250\,\mathrm{M}_\odot$, after a further collision with a main-sequence star. In contrast, when using SEVN, this PCP undergoes a PISN and does not leave a compact object. At the same metallicity, the SEVN prescriptions allow other two PCPs (with $M_{\rm max} \simeq 375$ and $\simeq 430\,\mathrm{M}_\odot$, respectively) to form two IMBHs with mass $M_{\rm rem} \simeq 150\,\mathrm{M}_\odot$, while the extrapolated fitting formulas used in Mapelli (2016) predict the formation of two lighter BHs (mass below $\sim 40\,\mathrm{M}_\odot$).

At $Z = 2.0 \times 10^{-4}$ (right-hand panel), two PCPs of Mapelli (2016) form IMBHs with $M_{\rm rem} \simeq 215$ and $\simeq 140\,\mathrm{M}_\odot$, respectively. Using SEVN, these two PCPs do not collapse into IMBHs since they undergo a PISN. Similarly, our new models predict that the three PCPs with $M_{\rm max} \gtrsim 340\,{\rm M}_{\odot}$ avoid a PISN and collapse into IMBHs, with masses above $\sim$300 $\rm M_{\odot}$.

Fig. 6 shows that PPISNe, PISNe and up-to-date stellar evolution models for VMSs (Chen et al. 2015) can significantly affect the evolution of the PCP. This suggests that a set of self-consistent *N*-body simulations including SEVN is absolutely necessary to get more insights on the runaway collision mechanism, and will be performed in a follow-up paper.

The bottom line of our preliminary study is that no IMBHs can form at solar metallicity from runaway collisions (in good agreement with Mapelli 2016), while ∼20–30 per cent of runaway collision products can collapse to IMBHs at $Z \le 0.002$ (Mapelli 2016 predicts that ∼10–20 per cent of runaway collision products can form IMBHs at $Z \le 0.002$).

5 SUMMARY

We described an updated version of our population synthesis code, SEVN, where we included an analytical prescription for PPISNe and PISNe (derived from Woosley 2017) and up-to-date stellar evolution tracks for VMSs, with $M_{\rm ZAMS}$ up to $350\,{\rm M}_{\odot}$ (Chen et al. 2015). The new version of SEVN is publicly available and can be downloaded from http://web.pd.astro.it/mapelli/group.html#software or https://gitlab.com/mario.spera/SEVN.

We used the new version of SEVN to study the BH mass spectrum at different metallicities, ranging from $Z = 2.0 \times 10^{-4}$ to 2.0×10^{-2}. We find that the effect of PPISNe becomes significant for $Z \le 2.0 \times 10^{-3} \simeq 0.1\,{\rm Z}_{\odot}$, for stars with $60 \le M_{\rm ZAMS}/{\rm M}_{\odot} \le 125$. PISNe are effective in the range $1.0 \times 10^{-3} \le Z \le 8.0 \times 10^{-3}$ for stars with $150 \le M_{\rm ZAMS}/{\rm M}_{\odot} \le 350$ (the lower mass limit slightly depending on metallicity). For $Z \lesssim 1.0 \times 10^{-3} \simeq 0.07\,{\rm Z}_{\odot}$, VMSs do not undergo a PISN and collapse directly to IMBHs with mass $\gtrsim 200\,{\rm M}_{\odot}$.

Moreover, PPISNe and PISNe enhance the formation of BHs in the mass range $30 \le M_{\rm rem}/{\rm M}_{\odot} \le 50$, while preventing the formation of compact remnants with mass $60 \le M_{\rm rem}/{\rm M}_{\odot} \le 120$. This implies that PPISNe and PISNe favour the formation of BHs with mass between 25 and $50\,{\rm M}_{\odot}$, i.e. in the mass range of the GW150914 ($m_1 = 36.2^{+5.2}_{-3.8}\,{\rm M}_{\odot}$ and $m_2 = 29.1^{+3.7}_{-4.4}\,{\rm M}_{\odot}$). From our simulations, we estimated that GW150914 and GW170104 likely formed in a metal-poor environment with metallicity $Z \le 0.3\,{\rm Z}_{\odot}$ (see also Abbott et al. 2016d and Belczynski et al. 2016a) and $Z \le 0.5\,{\rm Z}_{\odot}$, respectively.

Finally, we discuss the formation of IMBHs from VMSs. We studied the impact of PPISNe and PISNe on the runaway collision products formed in the direct *N*-body simulations of Mapelli (2016), who do not include the effect of PPISNe and PISNe. In our simulations, no IMBHs form from runaway collisions of metal-rich stars ($Z = 0.02$), in agreement with Mapelli (2016). In metal-poor star clusters, we find that ∼20–30 per cent of runaway collision products collapse to IMBHs (Mapelli 2016 finds ∼10–20 per cent). There are significant differences in the fate of each single collision product between this paper and Mapelli (2016). These differences arise from the different recipes adopted for the evolution of VMSs, from the effect of PPISNe and PISNe, but also from the fact that we do not integrate the dynamical evolution of the collision products. Thus, in a forthcoming paper, we will perform a set of self-consistent *N*-body simulations including the new version of SEVN to shed light on the formation of IMBHs from VMSs in star clusters.

ACKNOWLEDGEMENTS

We thank the anonymous referee for their comments, which helped us to improve the manuscript. We thank Alessandro Bressan for his invaluable suggestions and useful discussions. MM and MS acknowledge financial support from the Italian Ministry of Education, University and Research (MIUR) through grant FIRB 2012 RBFR12PM1F and from INAF through grant PRIN-2014-14. MM acknowledges support from the MERAC Foundation. Part of the Numerical calculations have been made possible through a CINECA-INFN agreement, providing access to resources on GALILEO and MARCONI at CINECA.

REFERENCES

Abbott B. P. et al., 2016a, Phys. Rev. X, 6, 041015
Abbott B. P. et al., 2016b, Phys. Rev. Lett., 116, 061102
Abbott B. P. et al., 2016c, Phys. Rev. Lett., 116, 241103
Abbott B. P. et al., 2016d, ApJ, 818, L22
Abbott B. P. et al., 2017, Phys. Rev. Lett., 118, 221101
Barkat Z., Rakavy G., Sack N., 1967, Phys. Rev. Lett., 18, 379
Baumgardt H., 2017, MNRAS, 464, 2174
Belczynski K., Bulik T., Fryer C. L., Ruiter A., Valsecchi F., Vink J. S., Hurley J. R., 2010, ApJ, 714, 1217
Belczynski K., Holz D. E., Bulik T., O'Shaughnessy R., 2016a, Nature, 534, 512
Belczynski K. et al., 2016b, A&A, 594, A97
Bond J. R., Arnett W. D., Carr B. J., 1984, ApJ, 280, 825
Bonnell I. A., Bate M. R., Zinnecker H., 1998, MNRAS, 298, 93
Bressan A., Marigo P., Girardi L., Salasnich B., Dal Cero C., Rubele S., Nanni A., 2012, MNRAS, 427, 127
Caffau E., Ludwig H.-G., Steffen M., Freytag B., Bonifacio P., 2011, Sol. Phys., 268, 255
Capuzzo-Dolcetta R., Spera M., Punzo D., 2013, J. Comput. Phys., 236, 580
Casares J., Jonker P. G., 2014, Space Sci. Rev., 183, 223
Chamel N., Haensel P., Zdunik J. L., Fantina A. F., 2013, Int. J. Mod. Phys. E, 22, 1330018
Chen Y., Bressan A., Girardi L., Marigo P., Kong X., Lanza A., 2015, MNRAS, 452, 1068
Chen K.-J., Woosley S., Heger A., Almgren A., Whalen D. J., 2014, ApJ, 792, 28
Cooke J. et al., 2012, Nature, 491, 228
Crowther P. A. et al., 2016, MNRAS, 458, 624
Ertl T., Janka H.-T., Woosley S. E., Sukhbold T., Ugliano M., 2016, ApJ, 818, 124
Farr W. M., Sravan N., Cantrell A., Kreidberg L., Bailyn C. D., Mandel I., Kalogera V., 2011, ApJ, 741, 103
Farrell S. A., Webb N. A., Barret D., Godet O., Rodrigues J. M., 2009, Nature, 460, 73
Fowler W. A., Hoyle F., 1964, ApJS, 9, 201
Freitag M., Gürkan M. A., Rasio F. A., 2006, MNRAS, 368, 141
Fryer C. L., 1999, ApJ, 522, 413
Fryer C. L., Kalogera V., 2001, ApJ, 554, 548
Fryer C. L., Belczynski K., Wiktorowicz G., Dominik M., Kalogera V., Holz D. E., 2012, ApJ, 749, 91
Gal-Yam A. et al., 2009, Nature, 462, 624
Giersz M., Leigh N., Hypki A., Lützgendorf N., Askar A., 2015, MNRAS, 454, 3150
Gräfener G., Hamann W.-R., 2008, A&A, 482, 945
Heger A., Fryer C. L., Woosley S. E., Langer N., Hartmann D. H., 2003, ApJ, 591, 288
Janka H.-T., 2012, Annual Review of Nuclear and Particle Science, 62, 407
Kızıltan B., Baumgardt H., Loeb A., 2017, Nature, 542, 203
Kozyreva A. et al., 2017, MNRAS, 464, 2854
Kroupa P., 2001, MNRAS, 322, 231
Lanzoni B. et al., 2013, ApJ, 769, 107
Lützgendorf N. et al., 2013, A&A, 552, A49

Mapelli M., 2016, MNRAS, 459, 3432
Mapelli M., Colpi M., Zampieri L., 2009, MNRAS, 395, L71
Mapelli M., Zampieri L., Ripamonti E., Bressan A., 2013, MNRAS, 429, 2298
Muijres L. E., Vink J. S., de Koter A., Müller P. E., Langer N., 2012, A&A, 537, A37
O'Connor E., Ott C. D., 2011, ApJ, 730, 70
Ober W. W., El Eid M. F., Fricke K. J., 1983, A&A, 119, 61
Oppenheimer J. R., Volkoff G. M., 1939, Phys. Rev., 55, 374
Özel F., Psaltis D., Narayan R., McClintock J. E., 2010, ApJ, 725, 1918
Paxton B. et al., 2013, ApJS, 208, 4
Paxton B. et al., 2015, ApJS, 220, 15
Portegies Zwart S. F., McMillan S. L. W., 2002, ApJ, 576, 899
Portegies Zwart S. F., Makino J., McMillan S. L. W., Hut P., 1999, A&A, 348, 117
Portegies Zwart S. F., McMillan S. L. W., Hut P., Makino J., 2001, MNRAS, 321, 199
Portegies Zwart S. F., Baumgardt H., Hut P., Makino J., McMillan S. L. W., 2004, Nature, 428, 724
Smartt S. J., 2015, PASA, 32, e016
Spera M., Mapelli M., Bressan A., 2015, MNRAS, 451, 4086
Spera M., Mapelli M., Jeffries R. D., 2016, MNRAS, 460, 317
Strader J., Chomiuk L., Maccarone T. J., Miller-Jones J. C. A., Seth A. C., Heinke C. O., Sivakoff G. R., 2012, ApJ, 750, L27
Tang J., Bressan A., Rosenfield P., Slemer A., Marigo P., Girardi L., Bianchi L., 2014, MNRAS, 445, 4287
Timmes F. X., Woosley S. E., Weaver T. A., 1996, ApJ, 457, 834
Vink J. S., 2016, preprint (arXiv:1610.00578)
Vink J. S., de Koter A., Lamers H. J. G. L. M., 2001, A&A, 369, 574
Vink J. S., Muijres L. E., Anthonisse B., de Koter A., Gräfener G., Langer N., 2011, A&A, 531, A132
Woosley S. E., 2017, ApJ, 836, 244 (W17)
Woosley S. E., Heger A., Weaver T. A., 2002, Rev. Mod. Phys., 74, 1015
Woosley S. E., Blinnikov S., Heger A., 2007, Nature, 450, 390
Yoshida T., Umeda H., Maeda K., Ishii T., 2016, MNRAS, 457, 351
Zocchi A., Gieles M., Hénault-Brunet V., 2017, MNRAS, 468, 4429

APPENDIX A: A NEW METHOD TO INTERPOLATE STELLAR EVOLUTION TRACKS IN SEVN

The old version of SEVN evolves a star with $M_{\rm ZAMS,s} = M_{\rm s}$ and metallicity $Z_{\rm s}$ by interpolating the pre-evolved tracks of two stars with $M_{\rm ZAMS,\,1} = M_1 = M_{\rm s} - \Delta M$ and $M_{\rm ZAMS,\,2} = M_2 = M_{\rm s} + \Delta M$, respectively, where ΔM is the step of the mass grid in the input tables. The mass of the star at time $t = \widetilde{t}$ is obtained by linear interpolation:

$$M_{\rm s}\left(t = \widetilde{t}\right) = \alpha_1 M_1\left(t = \widetilde{t}\right) + \alpha_2 M_2\left(t = \widetilde{t}\right), \qquad \text{(A1)}$$

where $\alpha_1 \equiv \frac{M_2 - M_{\rm s}}{M_2 - M_1}$ and $\alpha_2 \equiv \frac{M_{\rm s} - M_1}{M_2 - M_1}$.

Instead, the new version of SEVN uses the following algorithm. To evolve the star s at time $t = \widetilde{t}$, the new version of SEVN evaluates the value $p = \frac{\widetilde{t}}{t_{\rm life,s}}$, where $t_{\rm life,\,s}$ is the lifetime of the star s. $M_{\rm s}\left(t = \widetilde{t}\right)$ is calculated as

$$M_{\rm s}\left(t = \widetilde{t}\right) = \beta_1 M_1\left(t = \widetilde{t}_1\right) + \beta_2 M_2\left(t = \widetilde{t}_2\right), \qquad \text{(A2)}$$

where $\widetilde{t}_1 \equiv p t_{\rm life,1}$, $\widetilde{t}_2 \equiv p t_{\rm life,2}$, $\beta_1 \equiv \frac{M_1(M_2 - M_{\rm s})}{M_{\rm s}(M_2 - M_1)}$ and $\beta_2 \equiv \frac{M_2(M_{\rm s} - M_1)}{M_{\rm s}(M_2 - M_1)}$. This new approach ensures that the interpolating stars are in the same stellar phase of the target star s, and that the values of their physical parameters are appropriately weighted. This allows us to include less points in the input tables while reducing the interpolation error, as shown by Figs A1 and A2.

These figures show a comparison between the new and the old interpolation method to approximate the temporal evolution of the mass (Fig. A1) and the Helium core radius (Fig. A2) of a star with mass $M_{\rm ZAMS} = 70\,{\rm M}_{\odot}$ and metallicity $Z = 2.0 \times 10^{-2}$. It is apparent that the new interpolation method works much better than the previous one, especially for estimating the values of the physical parameters that are important for evolved stars (such as the Helium core radius).

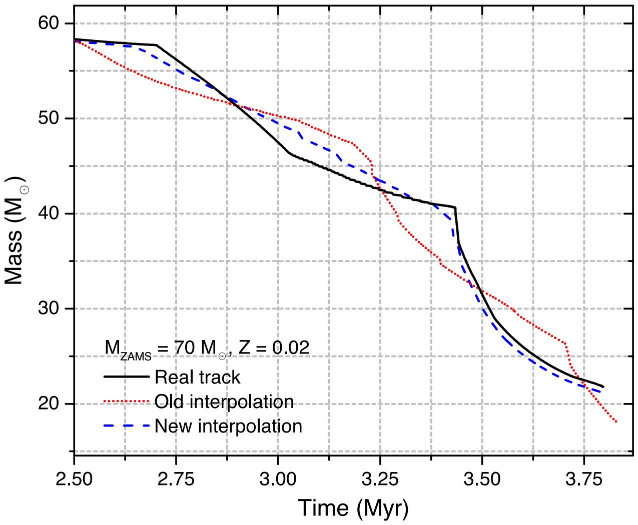

Figure A1. Time evolution of the mass of a star with $M_{\rm ZAMS} = 70\,{\rm M}_{\odot}$ at $Z = 2.0 \times 10^{-2}$. The black solid curve is obtained using the PARSEC stellar evolution code. Dotted red line: interpolation using the old version of SEVN; dashed blue line: new version of SEVN. Both the interpolated curves are obtained using the pre-evolved tracks of two stars with $M_1 = 60\,{\rm M}_{\odot}$ and $M_2 = 80\,{\rm M}_{\odot}$, respectively.

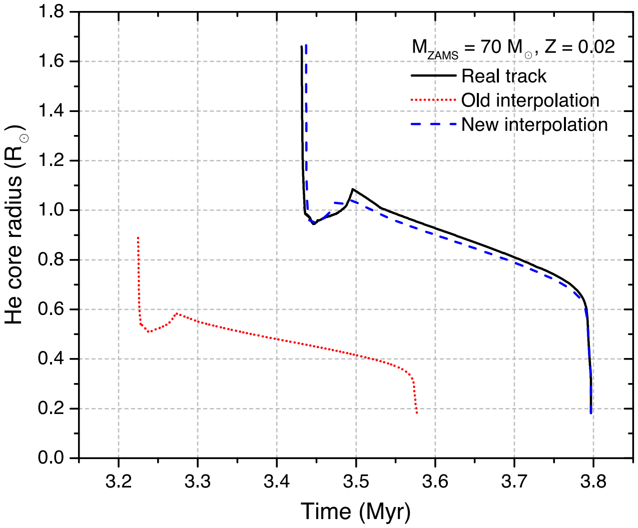

Figure A2. Same as Fig. A1 but for the time evolution of the Helium core radius.

It is worth noting that the new version of SEVN can also interpolate tables at different metallicity. That is, if the pre-evolved tracks are not available for the metallicity $Z_{\rm s}$, SEVN first evaluates $M_{\rm s}\left(t = \widetilde{t},\, Z = Z_1\right)$ and $M_{\rm s}\left(t = \widetilde{t},\, Z = Z_2\right)$, where $Z_1 \equiv Z_{\rm s} - \Delta Z$, $Z_2 \equiv Z_{\rm s} + \Delta Z$ and ΔZ is step in the metallicity grid. Then, the value $M_{\rm s}\left(t = \widetilde{t},\, Z_{\rm s}\right)$ is

$$M_{\rm s}\left(t = \widetilde{t},\, Z_{\rm s}\right) = \gamma_1 M_{\rm s}\left(t = \widetilde{t}_1,\, Z = Z_1\right) + \gamma_2 M_{\rm s}\left(t = \widetilde{t}_2,\, Z = Z_2\right), \qquad \text{(A3)}$$

where $\gamma_1 \equiv \frac{Z_{\rm s} - Z_1}{Z_2 - Z_1}$ and $\gamma_2 \equiv \frac{Z_2 - Z_{\rm s}}{Z_2 - Z_1}$.

APPENDIX B: THE FITTING FORMULA FOR PPISNE AND PISNE

The new version of SEVN includes a fitting formula to derive $M_{\rm rem}$ accounting for PPISNe and PISNe. This formula has been obtained by fitting the masses of the compact remnants shown in tables 1 and 2 of Woosley (2017) as a function of the final Helium mass fraction and of the Helium core mass $M_{\rm He,f}$ of the stars. Using the following fitting formulas, we get the parameter $\alpha_{\rm P}$ so that $M_{\rm rem} = \alpha_{\rm P} M_{\rm rem,\, no\, psn}$, where $M_{\rm rem,\, no\, psn}$ is the mass of the compact remnant we would obtain without PPISN/PISN (see equation 1). First, we define the following quantities

$$\begin{aligned} \mathcal{F} &\equiv \frac{M_{\rm He,f}}{M_{\rm fin}}, \\ \mathcal{K} &\equiv 0.67000\mathcal{F} + 0.10000, \\ \mathcal{S} &\equiv 0.52260\mathcal{F} - 0.52974. \end{aligned} \qquad \text{(B1)}$$

We then express $\alpha_{\rm P}$ as a function of $\mathcal{F}$, $\mathcal{S}$, $\mathcal{K}$ and $M_{\rm He,f}$:

$$\alpha_{\rm P} = \begin{cases} 1 \\ \quad \text{if } M_{\rm He,f} \le 32\,{\rm M}_{\odot},\ \forall \mathcal{F},\ \forall \mathcal{S} \\ 0.2\,(\mathcal{K} - 1)\, M_{\rm He,f} + 0.2\,(37 - 32\mathcal{K}) \\ \quad \text{if } 32 < M_{\rm He,f}/{\rm M}_{\odot} \le 37,\ \mathcal{F} < 0.9,\ \forall \mathcal{S} \\ \mathcal{K} \\ \quad \text{if } 37 < M_{\rm He,f}/{\rm M}_{\odot} \le 60,\ \mathcal{F} < 0.9,\ \forall \mathcal{S} \\ \mathcal{S}\left(M_{\rm He,f} - 32\right) + 1 \\ \quad \text{if } M_{\rm He,f} \le 37\,{\rm M}_{\odot},\ \mathcal{F} \ge 0.9,\ \forall \mathcal{S} \\ 5\mathcal{S} + 1 \\ \quad \text{if } 37 < M_{\rm He,f}/{\rm M}_{\odot} \le 56,\ \mathcal{F} \ge 0.9,\ \mathcal{S} < 0.82916 \\ (-0.1381\mathcal{F} + 0.1309)\left(M_{\rm He,f} - 56\right) + 0.82916 \\ \quad \text{if } 37 < M_{\rm He,f}/{\rm M}_{\odot} \le 56,\ \mathcal{F} \ge 0.9,\ \mathcal{S} \ge 0.82916 \\ -0.103645 M_{\rm He,f} + 6.63328 \\ \quad \text{if } 56 < M_{\rm He,f}/{\rm M}_{\odot} < 64,\ \mathcal{F} \ge 0.9,\ \forall \mathcal{S} \\ 0 \\ \quad \text{if } 64 \le M_{\rm He,f}/{\rm M}_{\odot} < 135,\ \forall \mathcal{F},\ \forall \mathcal{S} \\ 1 \\ \quad \text{if } M_{\rm He,f} \ge 135\,{\rm M}_{\odot},\ \forall \mathcal{F},\ \forall \mathcal{S}. \end{cases} \qquad \text{(B2)}$$

APPENDIX C: COMPARISON WITH W17

In this appendix, we compare our results with those presented in Woosley (2017).

Fig. C1 is a detail of Fig. 2, where we also plot the compact remnant masses taken from table 2 of W17 (black points). W17 explores the evolution of stars at $Z \simeq 0.1\,{\rm Z}_{\odot}$ in the mass range $70 < M_{\rm ZAMS}/{\rm M}_{\odot} < 150$, also varying the amount of mass-loss through stellar winds to mimic the results expected from stars at lower metallicity. The fitting formula we implemented in SEVN gives results in agreement with those of W17. We obtain a comparable maximum BH mass (this work:$\sim$55 ${\rm M}_{\odot}$, W17: 58 ${\rm M}_{\odot}$) and a similar mass range where a dearth of compact remnants is observed (this work: $55 \lesssim M_{\rm rem}/M_{\rm ZAMS} \lesssim 120$, W17: $58 < M_{\rm rem}/{\rm M}_{\odot} < 133$). The differences between this work and W17 are due to the parameters $M_{\rm He,f}$ and $\mathcal{F}$ used for the PPISNe and PISNe fitting formula (see Appendix B). Indeed, the values of $M_{\rm He,f}$ and $M_{\rm fin}$, for different $M_{\rm ZAMS}$ and metallicity, strongly depend on the adopted stellar evolutionary models.

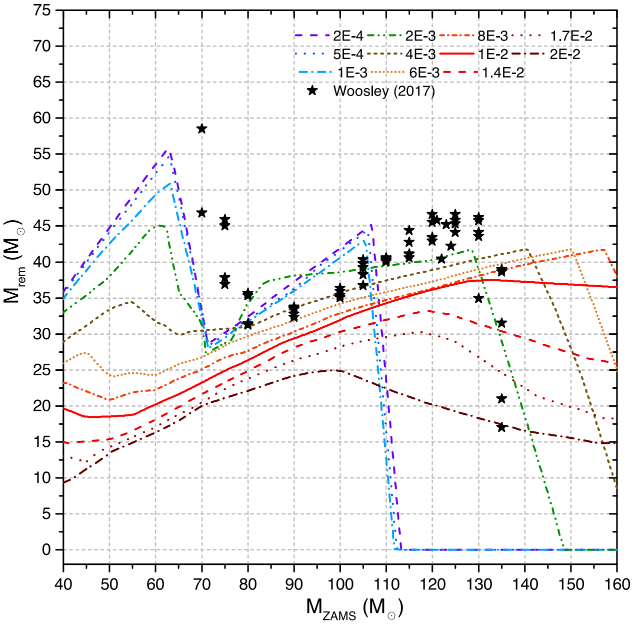

Figure C1. A detail of Fig. 2 that shows the ranges $40 \le M_{\rm ZAMS}/{\rm M}_{\odot} \le 160$ and $0 \le M_{\rm rem}/{\rm M}_{\odot} \le 75$. Black points are the compact remnant masses taken from table 2 of Woosley (2017).

APPENDIX D: STELLAR EVOLUTION TABLES

Tables D1, D2 and D3 show the final parameters of various progenitor stars and the mass of their compact remnants when PPISNe and PISNe are turned on and when PPISNe and PISNe are switched off in SEVN, for $Z = 2.0 \times 10^{-2}$, 2.0×10^{-3} and 2.0×10^{-4}, respectively. The adopted SN explosion mechanism is the delayed model and the stellar evolution tracks come from the PARSEC code.

Table D1. Final properties of stars of different initial mass and $Z = 2.0 \times 10^{-2}$ calculated with SEVN. $M_{\rm ZAMS}$: initial mass; $M_{\rm fin}$: final mass; $M_{\rm He,f}$: final Helium core mass; $M_{\rm CO,f}$: final Carbon–Oxygen core mass; $M_{\rm rem}$(no PSNe): mass of the compact remnant when PPISNe and PISNe are switched off; $M_{\rm rem}$: mass of the compact remnant. All values are given in $\mathrm{M}_{\odot}$.

$M_{\rm ZAMS}$	$M_{\rm fin}$	$M_{\rm He,f}$	$M_{\rm CO,f}$	$M_{\rm rem}$ (no PSNe)	$M_{\rm rem}$
8.0	8.0	2.2	1.2	1.3	1.3
13.8	13.0	4.5	2.6	1.3	1.3
19.5	17.1	6.9	4.4	3.4	3.4
25.2	19.9	9.8	6.4	8.1	8.1
31.0	16.0	12.6	8.8	10.7	10.7
36.8	13.1	13.1	9.5	9.8	9.8
42.5	13.4	13.4	9.6	10.2	10.2
48.2	14.7	14.7	10.6	12.6	12.6
54.0	16.3	16.3	11.7	14.6	14.6
59.8	18.1	18.1	13.1	16.3	16.3
65.5	20.2	20.2	14.5	18.2	18.2
71.2	22.6	22.6	16.2	20.3	20.3
77.0	23.9	23.9	17.2	21.5	21.5
82.8	25.2	25.2	18.1	22.7	22.7
88.5	26.6	26.6	19.1	23.9	23.9
94.2	27.4	27.4	19.7	24.7	24.7
100.0	27.7	27.7	19.8	25.0	25.0
105.8	26.1	26.1	18.7	23.5	23.5
111.5	24.5	24.5	17.6	22.1	22.1
117.2	23.0	23.0	16.5	20.7	20.7
123.0	21.7	21.7	15.6	19.5	19.5
128.8	20.4	20.4	14.7	18.4	18.4
134.5	19.3	19.3	13.9	17.4	17.4
140.2	18.4	18.4	13.2	16.5	16.5
146.0	17.5	17.6	12.7	15.8	15.8
151.8	16.7	16.9	12.2	15.0	15.0
157.5	16.5	16.5	11.9	14.8	14.8
163.2	16.4	16.4	11.9	14.8	14.8
169.0	16.4	16.4	11.8	14.7	14.7
174.8	16.3	16.3	11.8	14.7	14.7
180.5	16.3	16.3	11.7	14.7	14.7
186.3	16.2	16.2	11.7	14.6	14.6
192.0	16.2	16.2	11.7	14.6	14.6
197.8	16.2	16.2	11.7	14.5	14.5
203.5	16.1	16.1	11.6	14.5	14.5
209.2	16.1	16.1	11.6	14.5	14.5
215.0	16.2	16.2	11.7	14.6	14.6
220.8	16.2	16.2	11.7	14.6	14.6
226.5	16.2	16.2	11.7	14.6	14.6
232.2	16.2	16.2	11.7	14.6	14.6
238.0	16.2	16.2	11.7	14.6	14.6
243.8	16.3	16.3	11.7	14.6	14.6
249.5	16.3	16.3	11.7	14.7	14.7
255.2	16.4	16.4	11.8	14.7	14.7
261.0	16.5	16.5	11.9	14.8	14.8
266.8	16.6	16.6	11.9	14.9	14.9
272.5	16.7	16.7	12.0	15.0	15.0
278.2	16.8	16.8	12.1	15.1	15.1
284.0	16.9	16.9	12.2	15.2	15.2
289.8	17.0	17.0	12.2	15.3	15.3
295.5	17.0	17.0	12.3	15.3	15.3
301.2	17.0	17.0	12.3	15.3	15.3
307.0	17.0	17.0	12.3	15.3	15.3
312.8	17.0	17.0	12.3	15.3	15.3
318.5	17.0	17.0	12.3	15.3	15.3
324.2	17.0	17.0	12.2	15.3	15.3
330.0	17.0	17.0	12.2	15.3	15.3
335.8	16.9	16.9	12.2	15.2	15.2
341.5	16.9	16.9	12.2	15.2	15.2
350.0	16.9	16.9	12.2	15.2	15.2

Table D2. Same as Table D1 but for $Z = 2.0 \times 10^{-3}$.

$M_{\rm ZAMS}$	$M_{\rm fin}$	$M_{\rm He,f}$	$M_{\rm CO,f}$	$M_{\rm rem}$ (no PSNe)	$M_{\rm rem}$
8.0	8.0	2.5	1.3	1.3	1.3
13.8	13.7	4.8	2.7	1.4	1.4
19.5	19.2	7.3	4.6	4.1	4.1
25.2	24.7	10.1	6.6	10.4	10.4
31.0	29.7	13.1	8.9	19.9	19.9
36.8	34.3	16.2	11.4	30.9	30.9
42.5	38.0	19.4	13.7	34.2	34.2
48.2	41.2	22.8	16.2	37.1	37.1
54.0	45.4	26.2	18.6	40.9	40.9
59.8	49.8	29.9	21.3	44.8	44.8
65.5	49.5	34.4	24.5	44.5	35.4
71.2	52.4	37.3	26.6	47.2	27.2
77.0	46.0	41.7	29.8	41.4	29.9
82.8	45.6	45.1	31.9	41.1	36.6
88.5	47.3	47.3	34.0	42.6	38.0
94.2	48.0	48.0	34.8	43.2	38.3
100.0	48.6	48.6	35.2	43.8	38.6
105.8	49.7	49.7	35.9	44.8	39.1
111.5	50.8	50.8	36.7	45.7	39.6
117.2	51.8	51.8	37.4	46.6	40.0
123.0	53.6	53.6	38.9	48.2	40.8
128.8	56.1	56.1	41.0	50.5	41.4
134.5	58.5	58.5	43.0	52.7	30.0
140.2	60.8	60.8	45.0	54.7	18.1
146.0	63.0	63.0	46.9	56.7	5.7
151.8	65.2	65.2	48.7	58.7	0.0
157.5	67.4	67.4	50.2	60.6	0.0
163.2	69.4	69.4	51.6	62.5	0.0
169.0	71.5	71.5	53.0	64.3	0.0
174.8	73.4	73.4	54.3	66.1	0.0
180.5	75.3	75.3	55.5	67.8	0.0
186.3	77.1	77.1	56.8	69.4	0.0
192.0	78.9	78.9	57.9	71.0	0.0
197.8	80.7	80.7	59.2	72.6	0.0
203.5	82.6	82.6	60.8	74.4	0.0
209.2	84.9	84.9	62.9	76.4	0.0
215.0	87.1	87.1	64.9	78.4	0.0
220.8	89.2	89.2	66.9	80.3	0.0
226.5	91.3	91.3	68.9	82.2	0.0
232.2	93.3	93.3	70.8	84.0	0.0
238.0	95.3	95.3	72.7	85.8	0.0
243.8	97.2	97.2	74.6	87.5	0.0
249.5	99.2	99.2	76.4	89.3	0.0
255.2	101.3	101.3	78.1	91.2	0.0
261.0	103.5	103.5	79.6	93.1	0.0
266.8	105.6	105.6	81.1	95.1	0.0
272.5	107.7	107.7	82.5	97.0	0.0
278.2	109.8	109.8	83.9	98.8	0.0
284.0	111.8	111.8	85.3	100.6	0.0
289.8	113.8	113.8	86.7	102.4	0.0
295.5	115.7	115.7	88.0	104.1	0.0
301.2	117.7	117.7	89.6	105.9	0.0
307.0	119.7	119.7	91.4	107.7	0.0
312.8	121.7	121.7	93.3	109.5	0.0
318.5	123.6	123.6	95.2	111.3	0.0
324.2	125.6	125.6	97.0	113.0	0.0
330.0	127.5	127.5	98.9	114.7	0.0
335.8	129.3	129.3	100.7	116.4	0.0
341.5	131.1	131.1	102.5	118.0	0.0
350.0	132.4	132.4	103.3	119.2	0.0

Table D3. Same as Table D1 but for $Z = 2.0 \times 10^{-4}$.

$M_{\rm ZAMS}$	$M_{\rm fin}$	$M_{\rm He,f}$	$M_{\rm CO,f}$	$M_{\rm rem}$ (no PSNe)	$M_{\rm rem}$
8.0	8.0	2.5	1.4	1.3	1.3
13.8	13.7	4.8	2.8	1.4	1.4
19.5	19.5	7.2	4.5	4.0	4.0
25.2	25.2	10.1	6.7	10.7	10.7
31.0	31.0	13.2	9.1	21.3	21.3
36.8	36.7	16.4	11.5	33.0	33.0
42.5	42.4	19.7	14.0	38.1	38.1
48.2	48.0	23.2	16.6	43.2	43.2
54.0	53.7	26.8	19.2	48.3	48.3
59.8	59.3	30.3	21.8	53.4	53.4
65.5	64.6	33.5	24.2	58.2	48.5
71.2	70.1	37.0	26.7	63.1	28.8
77.0	75.3	40.3	29.2	67.7	31.1
82.8	79.5	44.1	32.0	71.5	33.8
88.5	83.1	48.3	35.2	74.8	36.6
94.2	88.1	51.9	37.8	79.3	39.2
100.0	94.0	55.5	40.3	84.6	41.9
105.8	100.0	59.3	43.5	90.0	44.8
111.5	105.7	63.0	46.8	95.2	12.5
117.2	111.2	66.5	49.8	100.1	0.0
123.0	116.9	70.1	52.8	105.2	0.0
128.8	122.8	73.8	55.6	110.5	0.0
134.5	128.5	77.3	58.3	115.6	0.0
140.2	133.9	80.8	60.8	120.5	0.0
146.0	139.0	84.1	63.3	125.1	0.0
151.8	144.5	87.6	66.0	130.1	0.0
157.5	150.5	91.3	69.1	135.4	0.0
163.2	156.3	95.1	72.1	140.7	0.0
169.0	161.9	98.7	75.1	145.8	0.0
174.8	167.4	102.2	77.9	150.7	0.0
180.5	172.7	105.6	80.7	155.4	0.0
186.3	177.8	108.9	83.5	160.0	0.0
192.0	182.7	112.1	86.1	164.5	0.0
197.8	187.7	115.4	88.9	168.9	0.0
203.5	192.9	118.8	91.8	173.6	0.0
209.2	198.4	122.5	95.1	178.6	0.0
215.0	203.9	126.1	98.3	183.5	0.0
220.8	209.2	129.7	101.5	188.2	0.0
226.5	214.3	133.2	104.6	192.9	0.0
232.2	219.3	136.5	107.7	197.4	197.4
238.0	224.2	139.9	110.7	201.8	201.8
243.8	229.0	143.2	113.7	206.1	206.1
249.5	233.8	146.4	116.6	210.4	210.4
255.2	238.9	150.1	119.3	215.0	215.0
261.0	244.1	153.7	122.0	219.7	219.7
266.8	249.1	157.3	124.6	224.2	224.2
272.5	254.1	160.9	127.1	228.7	228.7
278.2	259.0	164.3	129.6	233.1	233.1
284.0	263.7	167.8	132.0	237.3	237.3
289.8	268.4	171.1	134.4	241.5	241.5
295.5	272.9	174.5	136.8	245.6	245.6
301.2	277.7	178.0	139.7	249.9	249.9
307.0	282.3	181.5	142.7	254.1	254.1
312.8	287.0	185.2	146.0	258.3	258.3
318.5	291.6	188.7	149.3	262.4	262.4
324.2	296.1	192.2	152.6	266.5	266.5
330.0	300.6	195.7	155.8	270.5	270.5
335.8	304.9	199.1	159.0	274.4	274.4
341.5	309.3	202.1	162.2	278.3	278.3
350.0	311.6	204.4	165.4	281.2	281.2

This paper has been typeset from a TEX/LATEX file prepared by the author.